RESEARCH ARTICLE

Photocatalytic Films

Energy & Environmental Materials WILEY

Origin of Physicochemical and Mechanical Stability of Low-Temperature Prepared TiO_2-Based Photocatalytic Films: Surface Hydroxyl Density Matching

Andraž Šuligoj, Mohamad El-Roz, Goran Dražić, Frédéric Thibault-Starzyk, Pegie Cool, Nataša Zabukovec Logar, Urška Lavrenčič Štangar, and Nataša Novak Tušar**

Low-temperature prepared Titania (TiO_2)-based composite films are promising for photocatalytic applications. However, their practical deployment has been hindered by poor mechanical stability and the uncontrolled release of constituent nanoparticles into the environment. To overcome these limitations, colloidal TiO_2 nanoparticles (TiO_2-NP) and colloidal silica nanoparticles (SiO_2-NP) are used herein to produce nanoscale composite films, which additionally show also 80% higher photocatalytic rate towards toluene removal as compared to P25. Importantly such films exhibit enhanced mechanical robustness, as a consequence of the improved physicochemical stability, attributed to encapsulation of TiO_2-NP and SiO_2-NP within an amorphous SiO_2 matrix. The adhesive and cohesive integrity of the prepared colloidal TiO_2-SiO_2 composite films was evaluated using the ISO 15184:2012 standard for film hardness testing, and the results demonstrate superiority compared with commercial pure TiO_2 (powder or colloidal) and commercial TiO_2–mesoporous SiO_2 composite films. Characterization reveals that interfacial interactions, particularly between surface hydroxyl groups (Si–OH and Ti–OH), drive this enhanced stability. The presented results indicate a novelty of this research in two directions: 1) proof of superiority in the mechanical stability of the prepared material; 2) explanation of the origin of the superiority in the mechanical stability of the prepared material. The findings offer a viable route to robust, economically efficient, environmentally friendly TiO_2 composite films suitable for scalable deployment in air and water purification systems or self-cleaning surfaces, addressing key limitations of conventional powder-based methods.

1. Introduction

Beyond the widely recognized global challenges of climate change, biodiversity collapse, and biogeochemical disruption, environmental pollution, particularly by persistent organic contaminants, remains a critical anthropogenic impact on ecosystems. Among current remediation strategies, technologies such as filtration, coagulation, microbial cleaning, and catalysis[1,2] are extensively used for treating both air and aquatic environments.

Photocatalysis is emerging as a leading approach for degradation of organic pollutants in air and water,[3–11] due to its ability to harness semiconductor-driven redox reactions under ambient conditions.[12–14] Semiconductor-based photocatalysis offers a fundamentally different paradigm shift with the development of solar-driven photocatalytic technologies,[15–17] which are scalable and potentially able to safely remove pollutants.[18,19] Recent efforts focus on tuning photocatalytic activity via external fields,[20,21] expanding spectral responsiveness,[22] and resolving complexities of competing interfacial phenomena across solid–liquid–gas interfaces.

Photocatalysts need an appropriate electronic band structure, chemical stability, and surface properties to absorb the appropriate electromagnetic

Dr. A. Šuligoj, Prof. N. Z. Logar, Prof. N. N. Tušar
Department of Inorganic Chemistry and Technology, National Institute of Chemistry, Hajdrihova 19, 1000, Ljubljana, Slovenia
E-mail: natasa.n.tusar@ki.si
Dr. A. Šuligoj, Prof. U. L. Štangar
Faculty of Chemistry and Chemical Technology, University of Ljubljana, Večna pot 113, 1000, Ljubljana, Slovenia
E-mail: urska.lavrencic.stangar@fkkt.uni-lj.si
Dr. M. El-Roz, Prof. F. Thibault-Starzyk
Laboratoire Catalyse et Spectrochimie, Université de Caen Basse-Normandie, ENSICAEN CNRS, 6 Bd Maréchal Juin, 14050, Caen, France
Prof. G. Dražić
Department of Materials Chemistry, National Institute of Chemistry, Hajdrihova 19, 1000, Ljubljana, Slovenia
Prof. P. Cool
Laboratory of Adsorption and Catalysis, Department of Chemistry, University of Antwerp, Universiteitsplein 1, 2610, Wilrijk, Belgium
Prof. N. Z. Logar, Prof. N. N. Tušar
Graduate School, University of Nova Gorica, Vipavska 13, 5001, Nova Gorica, Slovenia
The ORCID identification number(s) for the author(s) of this article can be found under https://doi.org/10.1002/eem2.70452.

DOI: 10.1002/eem2.70452

irradiation and transform oxygen to highly reactive oxygen species (ROS).[23,24] Four major ROS are recognized, comprising superoxide anion radical ($^{\cdot}O_2^-$), hydrogen peroxide (H_2O_2), singlet oxygen ($^1O_2$), and hydroxyl radical ($^{\cdot}OH$). Titanium dioxide (TiO_2) is one of the most studied and widely used photocatalysts due to a combination of physicochemical, structural and electronic properties that make it highly effective for environmental and energy-related applications. TiO_2 has a wide bandgap (3.0–3.2 eV) which enables strong oxidative power under UV irradiation, generating highly reactive electron–hole pairs. It has high photostability allowing long-term use under light exposure. It is non-toxic and abundant; therefore, it is relatively low-cost. TiO_2 can also be modified to act under visible and IR light.[16,25]

Photocatalytic TiO_2 in powder or colloidal form can release TiO_2 nanoparticles (TiO_2-NPs) from the system, posing a potential hazard to human health. Therefore, immobilization in a film, without affecting their performance, is crucial.[26–28] Producing films from metal oxides (MO) has made great progress in recent decades where solution-phase processing is appealing and three main techniques for depositing MO films exist; spin-coating, spray-coating, and inkjet printing.[29] Yet, the latter generally relies on post-deposition heating and moderate mechanical pressures.[29,30] Scale up challenges relate to enhancing formulation stability, broadening process windows, and enhancing film uniformity.[29] We have showed that Na^+ can diffuse from the glass support when the films were synthesized at elevated temperatures (>400 °C)[31]—a problem that could only be resolved by applying a protective amorphous SiO_2.[31] Yet, the issue of physicochemical stability of TiO_2-SiO_2 photocatalytic films remained unexplored. While adhesion promotors, such as silanes, are frequently used to stabilize films during synthesis, the primary bonding mechanism is attributed to surface hydroxyl groups,[32] which enable effective surface wetting, intimate contact, and favorable dispersion interactions with the substrate. TiO_2, as well as many other catalytically relevant oxides, are abundant in their density of surface OH groups.[33] These groups present on the particle's surface impart inorganic reactivity, meaning they self-condense into oligomeric structures that form stable chemical bonds between dissimilar materials, enhancing adhesion.

In the case of mixed oxides Al_2O_3, SiO_2, and ZrO_2 have been shown to reduce aggregation of TiO_2 particles, increasing surface area and improving adsorption of contaminants.[34,35] Such networks of inorganic binder is fundamental for the mechanical integrity of NP aggregates although with sacrificing flexibility.[36] This provides a porous network with high permeability and light transparency and is thus considered a good candidate for TiO_2-NP encapsulation,[30] avoiding the need for use of surfactants such as Triton[37] or oleic acid[38] which require high temperatures for their removal. The successful use of inert fully hydrolyzed SiO_2 for the encapsulation of powdered TiO_2-NP by low-temperature synthesis has been demonstrated previously.[39,40] Next, we have shown that the use of colloidal TiO_2-NP, instead of powder-based TiO_2-NP, is advantageous in the synthesis of TiO_2-SiO_2 films. Colloidal TiO_2-NP facilitates the mixing of reactants and resulted in high homogeneity of NPs in the final sol.[41] As a result, the immobilization of TiO_2-SiO_2 film on the solid support was successfully carried out, however, with low physicochemical stability.

To date, the physicochemical stability of TiO_2-SiO_2 photocatalytic films remains relatively unexplored.[38–40] To investigate this issue, we have, therefore, attempted to encapsulate colloidal TiO_2 NPs in a silane-derived SiO_2 mesh, prepared at low temperatures (<150 °C) by sol–gel method. To increase the water stability and physicochemical stability of the mesh, different fully hydrolyzed SiO_2 NPs were added. First, we added pre-synthesized mesoporous silica in powder form to colloidal TiO_2-NPs, a well-known and commonly used procedure.[41,42] In the second, new approach described in this article, colloidal and, fully hydrolyzed SiO_2 was incorporated into TiO_2 during silane sol–gel synthesis, allowing precise control over surface area and morphology of nanoparticles interactions, which could then be systematically evaluated. To evaluate the photocatalytic performance, the materials were tested for the oxidation of toluene and formaldehyde, respective compounds of two major classes of indoor air pollutants (aromatic and aldehydes). A combination of X-ray diffraction, surface techniques, and spectroscopic and microscopic characterization of the fabricated photocatalytic TiO_2-SiO_2 films, combined with photocatalytic test results, provided insights into the origins of their enhanced physicochemical stability. This study not only demonstrates the fabrication of high-performance thin films, but more importantly establishes a general design principle: achieving an approximately 1:1 match between the surface hydroxyl densities of TiO_2 and SiO_2 is the key determinant of enhanced mechanical stability.

2. Results and Discussion

2.1. Formation of TiO_2-SiO_2 Films with Different SiO_2 Binders

In this study, we focus on TiO_2 in two forms: colloidal TiO_2 (AS) and powdered TiO_2 (P25), combined with various silica binders, including colloidal silica (7C), ordered mesoporous silica (SBA-15), and disordered mesoporous silica (KIL-2 and 7000).

The photocatalysts were prepared via low-temperature sol–gel synthesis in which partly hydrolyzed SiO_2 was used as an entrapping mesh, thus making it possible to incorporate various fully hydrolyzed SiO_2 sources (mesoporous—approach one, and colloidal—approach two). To create the SiO_2 encapsulating mesh, tetraethyl orthosilicate (TEOS) was partially hydrolyzed in ethanol before different fully hydrolyzed SiO_2 sources were added and mixed thoroughly. Finally, colloidal TiO_2 (grain size ≈10 nm, AS) or powdered TiO_2 (grain size ≈25 nm, P25) were added and diluted with alcohol to obtain a stable suspension. Our previous study has shown[43] that TiO_2:SiO_2 ratios are important for achieving high photocatalytic efficiencies. We thus utilized 1:1 molar ratio of titania:silica for initial tests and later studied the impact of the ratio on both photocatalytic efficiency and physicochemical stability.

In such synthesis, KIL-2 nano-sized spheres act as a scaffold. Their monodisperse spherical geometry and interparticle mesoporosity provide a well-defined, reproducible pore network that physically separates and stabilizes TiO_2 nanoparticles against sintering or aggregation. The result is a composite (AS/KIL2) with good surface area retention and high OH density. SBA-15 acts as an external support rather than a matrix. Because AS titania cannot enter the channels, TiO_2 sits on the outer surface of SBA-15 rods. This means dispersion depends on the external surface area of SBA-15, which is much lower than its total BET area (Figure S7, Table S1, Supporting Information). Nevertheless, AS/SBA15 shows excellent surface area retention and a notably red-shifted indirect band gap, suggesting some degree of Ti–O–Si interfacial interaction even in this geometry. Lastly, Ultrasil 7000 provides the least controlled dispersion environment. Its irregular, polydisperse aggregate structure means TiO_2 nanoparticles distribute unevenly—some regions are TiO_2-rich, others silica-rich, resulting in the relatively modest surface area and single broad pore distribution in AS/7000.

The formation of covalent Ti–O–Si bridges at the interface between P25 TiO_2 crystallites and the sol–gel SiO_2 matrix proceeds through heterocondensation between chemically distinct surface hydroxyl groups. At the synthesis pH of ~1.5, TiO_2 surface hydroxyls are protonated (≡Ti–OH_2^+), rendering surface Ti centers electrophilic and susceptible to nucleophilic attack by the silanol groups (Si–OH) of the TEOS-derived oligomers, yielding ≡Ti–O–Si ≡ bridges with concomitant release of water. This condensation is thermodynamically favorable, as bridging metal–oxygen–metal bonds carry significantly higher dissociation energies than the terminal surface hydroxyls they replace—a principle well-established in sol–gel chemistry[44] and supported by DFT calculations on Ti–O bond energetics.[45]

The suspensions were transformed into ≈6 µm thick films on glass carriers (240 × 12 × 2 mm^3 glass slides) via the doctor-blade technique[46] using 30 µm channel wire-wound rod (**Figure 1**a). Doctor-blade casting is one of the most widely used and reliable techniques in the industry,[47] capable of producing highly uniform films of various materials. During the deposition, mechanical shear promotes intimate contact between TiO_2 surfaces and the surrounding SiO_2 sol, while subsequent solvent evaporation concentrates reactive species within the thinning film and drives further heterocondensation alongside homocondensation of the TEOS oligomers into a cross-linked SiO_2 network that progressively encapsulates and immobilizes the TiO_2 particles.

Finally, the films were dried and cured in a furnace at 150 °C for 1 h, where residual hydrogen-bonded Si–OH···HO–Ti contacts are converted into fully covalent Ti–O–Si bridges, expelling physisorbed water, and densifying the amorphous SiO_2 mesh—all while remaining below the temperature threshold for anatase-to-rutile transformation or particle sintering, thereby preserving the crystalline integrity of P25 (Figure S3, Supporting Information). Repetition of deposition and thermal treatment across three cycles incrementally builds up the composite coating, each cycle extending SiO_2 encapsulation and forming additional Ti–O–Si bonds at previously inaccessible TiO_2 surface sites, until the target surface density of 1.0 mg cm^{-2} is reached.

2.2. Photocatalytic Performance and Physicochemical Stability of TiO_2-SiO_2 Films

The materials exhibited excellent photocatalytic performance with complete removal of toluene in less than 2 h and >90% degradation of formaldehyde within 1.5 h (see Figures S1 and S2, Supporting Information). The initial concentration of toluene was 50 ppm, which is below the Occupational Safety and Health Administration (OSHA) permissible exposure limit of 200 ppm expressed in 8 h exposure over a 40-h workweek.[48] Conversely, this concentration is close to the U.S. Environmental Protection Agency's no observed adverse effect level (NOAEL) of 34 ppm.[49] The reactions resulted in complete mineralization which was verified by stoichiometric CO_2 formation (Figure S2, Supporting Information) with no detectable intermediates, confirming quantitative conversion of toluene to CO_2 and H_2O.

Colloidal TiO_2 AS exhibited faster rates than powdered TiO_2 P25 (Figure 1b) in the photocatalytic decomposition of toluene,[41] as a consequence of small grain size, which in addition to good crystallinity enables high OH generation ability.[41,50] Next, the adsorption properties of the material were greatly enhanced by the addition of both SiO_2 sources (mesoporous and colloidal). This suggests the silica-titania layer on the surface is porous and that toluene is mainly adsorbing on the underlying silica layer. SiO_2 has been shown to promote the dispersion of TiO_2 nanoparticles and thus to improve the catalytic performance.[51] According to the majority of reports, toluene is photocatalytically oxidized primarily via holes (h^+, lifetime of few ns), while formaldehyde is photocatalytically oxidized via OH radicals (˙OH, lifetime ≈10 µs).[52,53] Yet, even for a porous SiO_2 thin film (pore diameter of 3–4 nm), the distance of ˙OH diffusion is just around 10 nm.[54] For effective photocatalysis, efficient diffusion of pollutants into the film is essential for their degradation. Thus, surface area alone is unlikely to be the primary limiting factor in

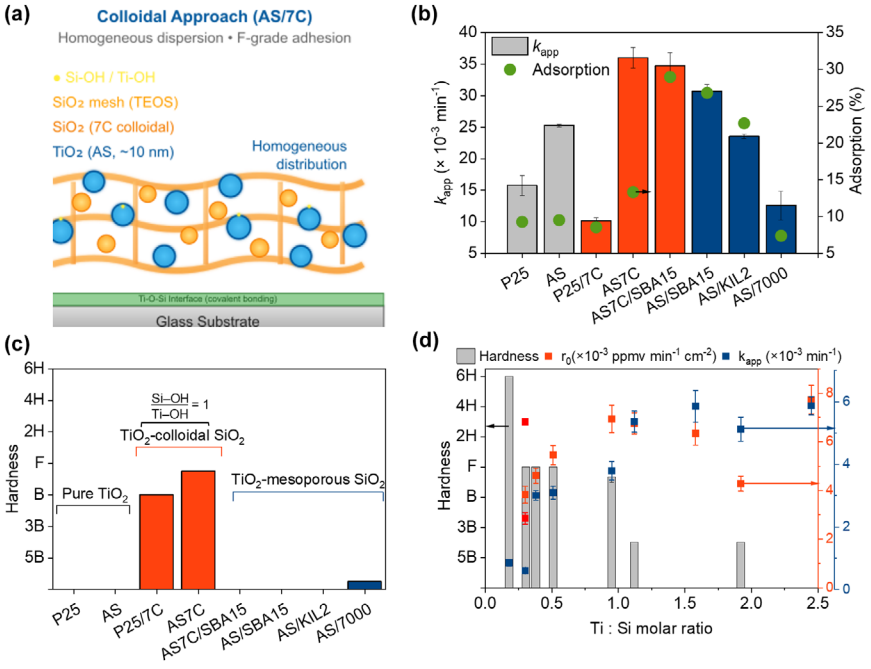

Figure 1. Scheme of films (a) and photocatalytic removal of toluene by TiO_2-SiO_2 samples (b–d). a) Note that the protective layer is not required in all cases and was not used in the current study. The interface is represented in blue and is formed via Si–O–Si bridges or via sintering when high temperature frit system is used. b) Removal via adsorption (circles) and decomposition (bars). c) Results of hardness testing according to the ISO 15184:2012 method. d) Activity towards toluene degradation and physicochemical stability of the sample AS/7C of various Ti:Si molar ratios. Error bars show standard error of the mean. The colors in facet (b) and (c) are identical. Samples are denoted: P25—powdered commercially available TiO_2, AS—colloidal commercially available TiO_2, 7C—synthesized colloidal SiO_2, SBA-15—synthesized ordered powdered SiO_2, KIL-2—synthesized disordered powdered SiO_2, 7000—commercially available disordered powdered SiO_2. Pencil hardness on the y-axis in (c) is graded on the European system using a continuum from H (for hardness) to B (for blackness), as well as F, a letter that was arbitrarily chosen to indicate midway between HB and H. Reaction conditions in (b): $m_{catalyst}$ = 65 mg, air flow = 400 mL min^{-1}, relative humidity = 50 ± 5%, T = 23 °C, $C_{0(toluene)}$ = 50 mg L^{-1}, Φ_{UVA} = 2.47 mW cm^{-2}.

formaldehyde oxidation. Instead, the key constraint appears to be pore accessibility, facilitating both pollutant and hydroxyl radical diffusion as demonstrated later in this study. All of this is preceded by the efficient absorption of incident photons which is not hindered by the presence of amorphous silica.[41] This is confirmed by efficient degradation of toluene in practically all composites apart from AS/7000. Importantly, the AS/7C composite exhibits ~80% higher toluene degradation rate compared to pure AS under identical conditions ($k = 0.057$ vs $0.031\ min^{-1}$), demonstrating that the colloidal SiO_2 matrix enhances rather than suppresses photocatalytic activity through improved TiO_2 dispersion and pollutant adsorption.

However, good photocatalytic performance is of limited value if the films lack the mechanical stability required for long term use.[55] The adhesive and cohesive integrity of the prepared colloidal TiO_2-SiO_2 composite films was evaluated using the ISO 15184:2012 standard for film hardness testing, and the results demonstrate superiority compared with commercial pure TiO_2 (powder or colloidal) and commercial TiO_2–mesoporous SiO_2 composite films. Samples containing colloidal SiO_2, P25/7C and AS/7C (Figure 1c) showed superior integrity ranging from F for AS/7C and B for P25/7C, while sample AS/7000 exhibited the lowest possible resistance, that is, 6B. Other samples (pure TiO_2—P25 and AS and TiO_2 mixtures with mesoporous SiO_2 SBA-15 and KIL-2) could not be tested due to their inadequate adhesion. We note that during the photocatalytic tests conducted in this study, all the films were of sufficient stability without any film loss during the course of photocatalytic tests. Furthermore, their photocatalytic activity was stable (Figure S1b, Supporting Information) and could be partially regained after a prolonged UV cleaning using clean air stream (Figures S1b and S11, Supporting Information). Real-time aerosol monitoring during photocatalytic testing confirmed that particle release decreased by >95% after an initial break-in period, with negligible nanoparticle shedding during subsequent operation (Figure S10, Supporting Information). This validates that mechanically stable films (F-grade hardness) retain TiO_2 nanoparticles during operational use.

To further elucidate the relationship between colloidal silica and colloidal titania (AS/7C), samples with Ti:Si molar ratios 0.2–3.0 were made (Figure 1d). A strong improvement in toluene photocatalytic rates activity was observed with increasing the Ti:Si molar ratio from 0.2 to 1.0 following a reverse exponential decay function ($y = y_0 + A_1 * \exp(-(x - x_0)/t_1)$, Supporting information). A plateau of highest reaction rate constant can thus be estimated ($y_0 = 0.057\ min^{-1}$) which is more than twice as high as the pure TiO_2, showcasing the influence of de-aggregating effect of silica in the composite. Conversely, the increment in TiO_2 loading decreased the mechanical stability substantially, with two large drops from 0.2 to 0.3 and 0.85 to 1.2 Ti:Si molar ratios. The optimum compromise between activity and physicochemical stability thus lies at a Ti:Si molar ratio of 0.85 (Figure 1d).

The optimal Ti:Si ratio of 0.85, rather than the stoichiometric 1:1 suggested by surface hydroxyl matching, reflects the operational reality that not all surface OH groups participate in Ti–O–Si bond formation—some remain sterically inaccessible or isolated, as later evidenced by TPD-IR measurements distinguishing accessible from total hydroxyl density (**Figure 2c**). This ratio represents the practical balance between photocatalytic activity (maximized by TiO_2 loading) and mechanical stability (requiring sufficient SiO_2 scaffold density for substrate adhesion).

2.3. Study of the Origin of Physicochemical Stability of TiO_2-SiO_2 Films

Since both the glass support and the mesoporous SiO_2 are amorphous and contain a high surface density of silanol groups, that act as sites for O–bridges with titanium, the adhesion of the film to the solid support should be determined by the adhesion of silica to glass (or other surfaces, if used). The addition of colloidal TiO_2 to various SiO_2 sources studied by FTIR spectroscopy (see Figure S6, Supporting Information) decreased the characteristic bands of the asymmetric Si–O–Si stretching vibration ($1070\ cm^{-1}$, referred to as Si–O–Si_{as}). This reflects the reduced interaction between SiO_2 parts due to the penetration of TiO_2 nanoparticles into the silica network. The band at $963\ cm^{-1}$ in combination with the band at $455\ cm^{-1}$ is characteristic of asymmetric Si–O–Ti stretching vibrations[56,57] and was observed in the composites AS/SBA15 and AS/7C (Figure 2a). This band could also be a superposition of Si–O stretching vibrations in Si–OH groups (silanol groups in the mesoporous materials), since all pure silica sources exhibit this peak, especially the disordered mesoporous silica 7000. However, a significant blue shift ($95\ cm^{-1}$) of the Si–O–Si_{as} peak to $1122\ cm^{-1}$ was observed only in the colloidal TiO_2:colloidal SiO_2 system (AS/7C). Combined with a decrease in the Si–O–Si_{as} band, this suggests a shift to less symmetric Si–O–Si group stretching. To confirm this, ATR-FTIR

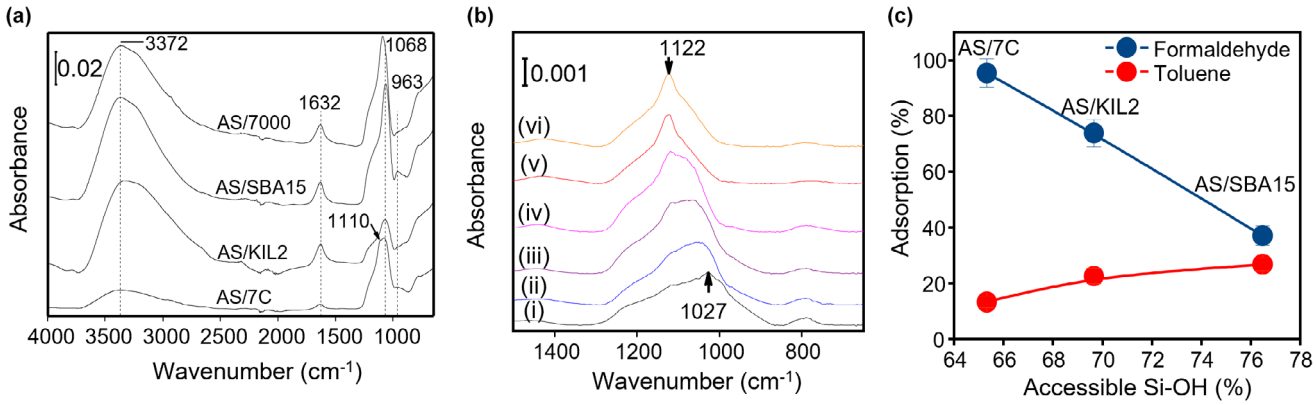

Figure 2. ATR-FTIR spectra and FTIR-derived silanol accessibility of various TiO_2-SiO_2 composites. a) Composites of all SiO_2 sources used. b) AS/7C composites of various Ti:Si molar ratios. c) Adsorption of formaldehyde and toluene with respect to measured Si–OH accessibility. In fact (b), the Ti:Si ratios are i) 0.2, ii) 0.4, iii) 0.6, iv) 1.2, v) 2.4, and vi) 3.0. Spectra are translated vertically for clarity.

spectra of AS/7C samples with different Ti:Si molar ratios were measured (Figure 2b). Higher Ti contents resulted in a shift of the Si–O–Si group from 1027 cm^{-1} to 1122 cm^{-1} for this band. Similarly, the intensity of the band at 800 cm^{-1} decreased and the Si–O–Si_{as} band became narrower, indicating less disorder and/or less strain. Such results are corroborated by Seki et al.,[58] who observed a blue shift in TO peak upon decreasing the thickness of SiO_2 layer on SiC support and ascribed the shift to increase in homogeneity in the SiO_2 phase. These results suggest an interaction of the TiO_2 particles with the silica matrix, progressive thinning of the SiO_2 mesh, and more effective entrapment of the TiO_2 particles in the silica matrix in AS/7C sample. It should be noted that an absolute quantification of the interfacial Si–O–Ti bonds is not feasible using FTIR spectroscopy in the present system. This limitation arises from the strong overlap of the vibrational bands associated with Si–O–Ti linkages with the much more intense and broad bands of the Si–O–Si and Ti–O–Ti frameworks in the same spectral region, which prevents reliable peak deconvolution and quantitative integration. Therefore, FTIR can only provide qualitative or at best semi-quantitative evidence for the formation of interfacial bonding, rather than an absolute number of Si–O–Ti linkages. While TPD-IR allows quantification of the accessible surface hydroxyl group density, it does not selectively distinguish hydroxyls directly associated with interfacial Si–O–Ti sites. Consequently, the role of interfacial bonding and hydroxyl matching is inferred from the combination of hydroxyl density measurements, structural characterization, and catalytic stability trends.

Particle size distribution and pore structures were characterized using transmission electron microscopy (TEM) and scanning electron microscopy (SEM), respectively. Films composed of pure AS titanium dioxide (see Figure S8b, Supporting Information) showed mesoporosity between particles. The AS/SBA-15 sample exhibited larger pores (18.2 nm) compared to pure mesoporous silica (9.2 nm)—a consequence of penetration of TiO_2 nanoparticles into the pores of the amorphous silica, which was also confirmed by TEM (Figure S8e, Supporting Information). The presence of smaller pores in this sample (6.2 nm) could be a consequence of the formation of new pores between the TiO_2 and SiO_2 phases within the mesopores of SBA-15. Also, the N_2 uptake data suggest that TiO_2 is entrapped within the pores of the disordered KIL-2 silica, as the pore radii are smaller (from 20 nm to 16.8 and 14 nm at entrapment [see Figure 5c, Supporting Information]). Conversely, the presence of mesopores in the AS/7C sample reflects the interparticle porosity of TiO_2, that is, titania NP is unlikely to be located within the pores of colloidal silica 7C. Overall, a very homogeneous distribution of TiO_2 NPs can be seen in sample AS/7C due to the spherical shape of colloidal SiO_2 (**Figure 3k**) and also in sample P25/7C. Due to the much smaller size of TiO_2 particles in AS (≈10 nm) compared to P25 (≈25 nm), the distribution is homogeneous.

High number of Si–O–Ti and/or ≡Si–OH···HO–Ti≡ bonds results in high number of anchoring points for TiO_2 NPs onto SiO_2 mesh. Additionally, it results in dense anchoring of the silica mesh onto the glass substrate, which in turn results in excellent mechanical stability. Forming many Si–O–Ti bonds require high number of surface OH per unit of surface area. We conducted a thermogravimetric analysis (TGA) of pure SiO_2 and pure TiO_2 samples (see Figure S5, Supporting Information) to determine surface OH concentration on these samples.[59] The value of surface OH for commercial disordered mesoporous SiO_2 (7000) was close to the value stated by the supplier (10.8 OH nm^{-2}). SBA-15, for instance, had surface Si–OH density of 3.47 OH nm^{-2} which is also in accordance with the literature values 3.4–3.5 OH nm^{-2}.[60,61] As expected, the disordered mesoporous SiO_2 KIL-2 had a slightly more hydroxylated surface (4.32 OH nm^{-2}) than SBA-15, which is due to its less ordered structure.[62] In contrast to our hypothesis, higher concentration of OH groups on the surface did not correlate to the physicochemical stability. Therefore, a ratio between the density of the surface OH of SiO_2 support and TiO_2 was calculated. This value was found closest to unity in AS/7C sample, where the ratio (silanol [7C]/titanol [AS]) density was 1.06, while in P25/7C it was 0.90. In all other composites, this ratio was 0.62 or lower. This aligns well with the N_2-sorption measurements, where the preservation of the pore structure was proven to be the most important parameter both in physicochemical and photocatalytic properties. Notably, other research also inferred local structural symmetry (spatially connected, coordinated local transformations to lower symmetry structures) was the most critical factor in predicting stability of glassy structures.[63,64] Therefore, colloidal silica with matching surface hydroxyl density to that of titania's was the most effective as an agent inside the SiO_2 entrapping network to stabilize titania NPs inside its structure.

We note that not all OH groups on the surface are involved in the SiO_2-TiO_2 interaction, nor in the adsorption of reactants on the surface.[65] Therefore, the amount of accessible, that is, non-isolated, hydroxyl groups on the surface (viz. silanol groups, ≡Si–OH) was investigated via TPD-IR using various molecular probes.[66] The adsorption properties of toluene increased with increasing amount of ≡Si–OH groups on the surface, whereas the trend was reversed for formaldehyde (Figure 2c). This indicates that the main adsorption sites for toluene are SiO_2 particles, while for formaldehyde these sites are on TiO_2. Therefore, the importance of pore structure and pore accessibility is much greater in the second case. Since the size of toluene (kinetic diameter = 0.67 nm) is larger than that of formaldehyde (0.24 nm),[67] one would expect the latter to diffuse more easily into the pores. In fact, the adsorption of formaldehyde was higher than that of toluene for all samples except the pure titanium dioxide sources. This indicates the best accessibility of the ≡Ti–OH sites in the AS/7C sample and lower accessibility in the samples with mesoporous silica. Since the pore structure in AS/7C and AS/SBA15 was maintained and the composite with SBA-15 had higher Si–OH accessibility, this is an indication that the number of surface silanol groups in 7C silica was reduced by the formation of Si–O–Ti bonds, as shown previously. This was the second function of colloidal SiO_2, that is, to improve the accessibility of surface titanols, which is essential for an efficient photocatalytic process. Unlike dense SiO_2 coatings that can block active sites and impede charge transfer,[68] the porous colloidal-based SiO_2 scaffold preserves TiO_2 accessibility (Figure 2c, TPD-IR) while providing additional pollutant adsorption capacity, resulting in synergistic activity enhancement.

If the matching of density of surface ≡Si–OH and ≡Ti–OH groups is crucial in particle distribution, this should reflect in the internal structure of the films. Cross-sectional images of the two most active samples (AS/7C and AS/SBA15) and their linear 50:50 combination (Figure 3) show that they differ largely in structure, that is, in sample AS/SBA15, large SiO_2 chunks are observed, which become progressively smaller as the proportion of SBA-15 in the total SiO_2 decreases.

In the sample AS/7C, the aggregates of silica are no longer visible, and the sample shows a highly uniform distribution of SiO_2 and TiO_2 particles, distinguishable only by elemental mapping. Note that the molar ratio between silica and titania is fixed at 1:1 in all cases. When the surface hydroxyl densities of TiO_2 and SiO_2 are mismatched (as in AS/SBA-15), like particles tend to self-aggregate, leading to phase separation—SiO_2 aggregates with SiO_2, forming the large chunks visible

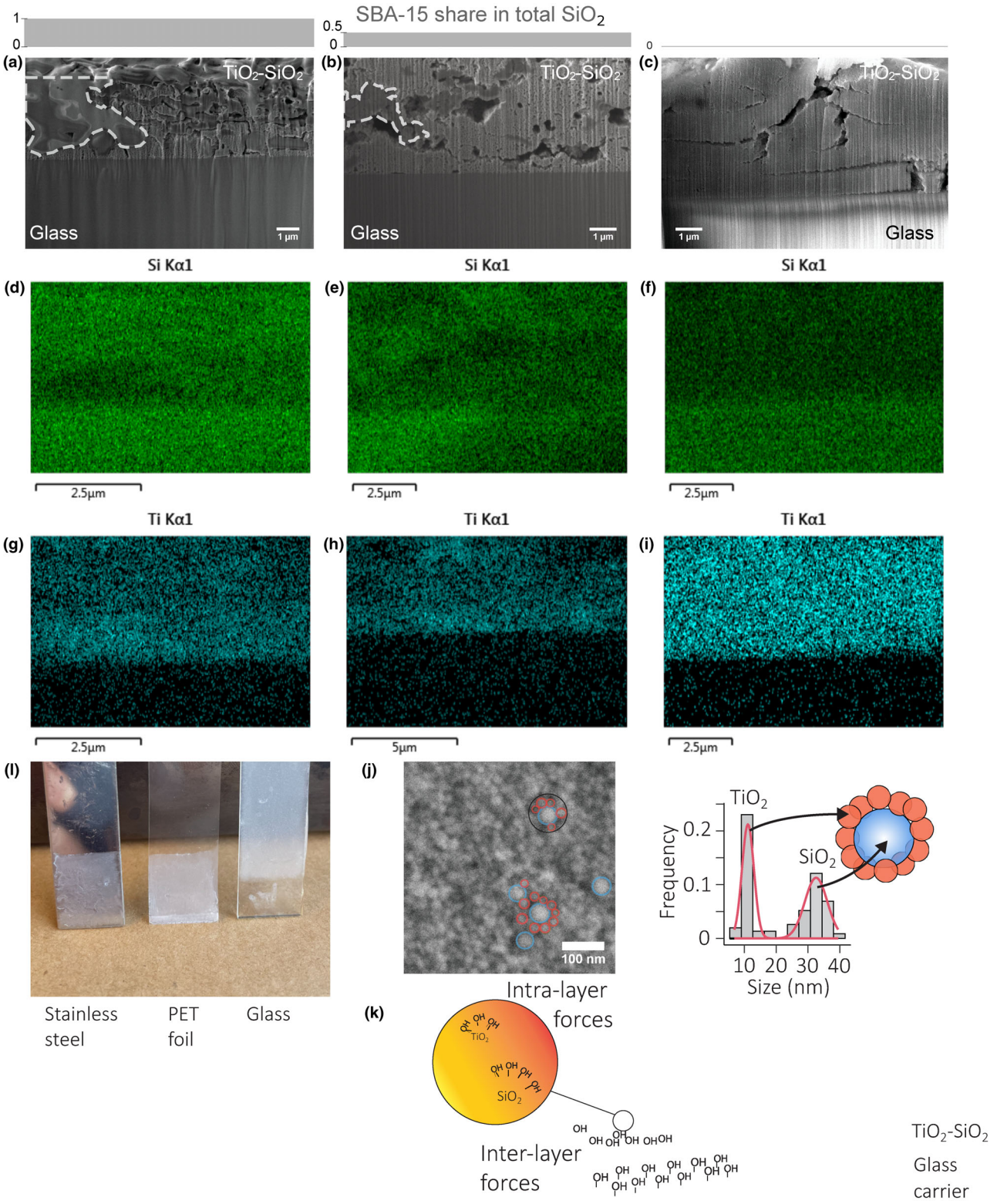

Figure 3. Electron microscopy imaging of samples. FIB-SEM micrographs of the two most active samples, AS/SBA15 (a, d, g) and AS/7C (c, f, i). In addition, the linear combination of the two, named AS/7C/SBA15 (b, e, h), is also shown. The elemental mappings of the corresponding samples are shown below each sample in subfigures (d–i). Note the large chunks of amorphous SiO_2 in the AS/SBA15 sample marked with a white dashed line. Top SEM image of AS/7C sample with the corresponding size distribution histogram (j). A schematic representation of the TiO_2-SiO_2 interface in intra- and inter-layer environment (k). Application of the concept to various surfaces (l).

in Figure 3a. Conversely, when the hydroxyl densities are matched (as in AS/7C with silanol:titanol ratio = 1.06), TiO_2 and SiO_2 particles uniformly cross-link with each other via hydroxyl condensation, forming a Ti–O–Si bond network that permeates the entire film. This results in homogeneous dispersion (Figure 3c,f,i) and superior mechanical interlocking. This can be further evidenced by the high physicochemical stability of the P25/7C sample, where P25 also has a compatible OH surface density to colloidal SiO_2 (ratio is 0.92, Table S1, Supporting Information). To further elaborate on this, we prepared two additional samples replacing SBA-15 in 50% AS/SBA-15 with CeO_2 or γ-Al_2O_3. Ceria showed OH density of 5 per nm^2 while alumina was measured at 8.9 OH nm^{-2} (Figure S5, Supporting Information). While the combination with SBA-15 showed inadequate mechanical stability due to OH mismatch, the same was true for CeO_2. On the other hand, replacing SBA-15 with alumina showed better mechanical integrity, which reached 5B level according to the ISO 15184:2012 test. However, we lowered OH on γ-Al_2O_3 via calcining at 300 °C thus reaching 7 OH nm^{-2}. In this case, the mechanical stability reached a much better level 2B, thus confirming the concept. It was surprising to find that the band gap values were elevated, especially for the composite with colloidal SiO_2 (from 3.05 eV for AS to 3.31 eV for AS/7C), since titania NPs were fully crystalline upon synthesizing the mixed oxide. The observed increase in band gap energy from 3.05 eV for pure TiO_2 to 3.31 eV in the TiO_2–SiO_2 composite cannot be attributed to quantum confinement, given the particle size (∼10 nm). Instead, diffuse reflectance spectroscopy revealed (Figure S4, Supporting Information) the lowest Urbach energy (E) for the TiO_2–SiO_2 material, indicating reduced structural disorder and suppression of defect-related band-tail states.[69] The incorporation of TiO_2 nanoparticles into the SiO_2 matrix likely promotes Ti–O–Si interfacial bonding, which passivates surface defects such as oxygen vacancies and Ti^{3+} centers. The reduction of sub-bandgap states sharpens the absorption edge and results in an apparent widening of the band gap. Thus, the increased Eg primarily reflects defect passivation and improved electronic ordering rather than size-induced quantum effects.

While direct carrier lifetime measurements were not performed, the passivation of recombination centers at Ti–O–Si interfaces, combined with enhanced activity, is consistent with maintained charge carrier utilization. Future TRPL/transient photocurrent studies would provide direct quantitative evidence.

This agrees with the FTIR measurements which indicate the interaction of SiO_2 and TiO_2 particles (Figure 2) when colloidal SiO_2 is used to aid entrapment in the amorphous SiO_2 mesh. To contextualize the performance of our low-temperature TiO_2–SiO_2 films, Table 1 compares mechanical stability (where available) and photocatalytic efficiency against literature TiO_2-based films. Since the studies of films are rare, some reports on other systems are also included. Critically, the AS/7C composite achieves F-grade pencil hardness (ISO 15184:2012) despite processing at only 150 °C—which is suitable for thermolabile substrates such as plastics on other organic polymers (Figure 3l). Remarkably, this mechanical enhancement does not compromise photocatalytic activity: the apparent first-order rate constant for toluene degradation ($k = 0.057\ min^{-1}$) exceeds most reported values in the literature, including pure P25 ($k = 0.022\ min^{-1}$, this work).

To provide a potential application, we constructed a pilot photocatalytic reactor constructed of four 8 W Philips Actinic BL lamps (365 nm broad max.) and 4 photocatalyst-coated glass slides ($305 \times 43 \times 4\ mm^3$). The photocatalyst was able to completely remove the incoming toluene with a quantitative transformation into CO_2, where, theoretically, the stoichiometric amount of CO_2 would be 8.4 ppmv whereas the steady-state concentration reached at the outlet of the reactor was hovering between 7 and 11 ppmv (**Figure 4**).

3. Conclusion

In summary, our findings demonstrate that the mechanical stability of TiO_2-SiO_2 photocatalytic films is primarily governed by the compatibility of surface hydroxyl groups between TiO_2 and SiO_2 nanoparticles. Selection of materials based on surface hydroxyl group density rather than particle size or morphology can prove most effective, with a 1:1 titanol-to-silanol ratio yielding optimal structural uniformity, a key parameter for industrial scalability. This configuration also ensures high accessibility of active sites to toluene and formaldehyde. The controlled combination of colloidal SiO_2 and TiO_2 can preserve the intrinsic pore architecture of titania and maintains efficient diffusion pathways for both pollutants and oxidative species ($^{\cdot}OH$, $O_2^{\cdot-}$). Future studies employing time-resolved photoluminescence and transient photocurrent spectroscopy would provide deeper insight into how interfacial Ti–O–Si bonds and elevated surface hydroxyl density influence photogenerated charge carrier lifetimes and separation efficiency.

4. Experimental Section

Materials: All chemicals in the present study were used as received without further purification. Absolute ethanol, hydrochloric acid (37%), formaldehyde solution (36.5%) were purchased from Sigma Aldrich, isopropanol and 1-propanol from Carlo Erba, tetraethyl orthosilicate, TEOS (95%) from Acros Organics, Levasil 200/30% from Obermeier and toluene from AppliChem. Degussa P25 photocatalyst and silica Ultrasil 7000 GR were purchased from Evonik, PC500 photocatalyst from Millennium, and CCA 100 AS photocatalysts were donated by Cinkarna Celje. Sol–gel silica was prepared separately. To TEOS (3.192 mL) colloidal Levasil 200/30% SiO_2 (4.62 mL) is added, followed by addition of HCl (0.0714 mL, 37%). Finally, isopropanol (13.6 mL) is added dropwise to the mixture while stirring. The solution should be left to stir at 300 rpm overnight at room temperature.

Mesoporous KIL-2 silica was synthesized according to the procedure described before,[80] as well as SBA-15 silica.[81]

For the purpose of this research 1.215 g of P25—a well-known benchmark TiO_2 catalyst—was suspended in 5 mL of water, followed by mixing at room temperature for 10 min at 300 rpm and sonication for 10 min under ambient conditions. The sample was labeled P25.

TiO_2-SiO_2 composites were made in Ti:Si molar ratio 1:1, where the appropriate amount of SiO_2 was added to titania source under ambient conditions and later mixed and sonicated as for the preparation of P25. The pH of such suspensions was ∼1.5, which is below the isoelectric point of silica (3–4), titania (5–6), and TiO_2-SiO_2 composites (3–4)[82] and, hence favored stable suspensions of both titania and silica, thus facilitated uniform mixing.

All catalysts were immobilized on glass ($240 \times 12 \times 2\ mm^3$), that was cleaned with ethanol, using a doctor-blade technique at room temperature with a Meyer rod that consisted of 25 µm grooves. Later, the coatings were thermally treated at 150 °C for 1 h. This process was repeated 3 times in order to obtain the surface density of the catalyst 1.0 mg cm^{-2}.[41] The doctor-blade method with a calibrated Meyer rod is widely recognized as providing excellent thickness reproducibility when process parameters are controlled—variations are typically <5% RSD in research-scale film preparation, as reported in the coating literature.[83]

The following process parameters insured reproducibility: 1) the doctor-blade technique employed used a Meyer rod with 25 µm grooves, which is a standardized coating tool that deterministically controls wet film thickness; 2) the coating speed was applied at consistent draw rate (5.0 cm s^{-1}); 3) the glass substrates were pre-treated, that is, cleaned with ethanol and dried before each coating; 4)

Table 1. Performance comparison with literature.

Materials	Synthesis method, temperature	Film thickness (μm)	Mechanical stability/ Adhesion	Chosen VOC	Degradation performance	References
Colloidal TiO_2 + colloidal SiO_2	Doctor-blade + sol–gel, 150 °C	~6	F-grade (ISO 15184)	Toluene (50 ppm)	$k = 0.057\ min^{-1}$, >95% removal (2 h)	—
P25 TiO_2 + colloidal SiO_2	Doctor-blade + sol–gel, 150 °C	~6	B-grade (ISO 15184)	Toluene (50 ppm)	$k \approx 0.025\ min^{-1}$, ~75% removal (2 h)	—
Pure colloidal TiO_2	Doctor-blade, 150 °C	~6	Untestable (poor)	Toluene (50 ppm)	$k = 0.031\ min^{-1}$, ~85% removal (2 h)	—
Pure P25 TiO_2	Doctor-blade, 150 °C	~6	Untestable (poor)	Toluene (50 ppm)	$k = 0.022\ min^{-1}$, ~70% removal (2 h)	—
P25 on glass fiber	Powder coating, 400 °C	NA	NA	Toluene (100 ppm)	~15–30% removal (1 h)[a]	[42]
P25 + Triton X-100	Spray-coating, 450 °C	NA	3B–4B (ISO 15184)	Formaldehyde (1 ppm)	~60% removal (3 h)[a]	[37]
TiO_2 on SiO_2-glass	Dip-coating, 500 °C	μm thick	NA	Toluene & acetaldehyde	Removal varies with film thickness	[70]
Mesoporous TiO_2	Sol–gel templating, 350–450 °C	Thin films	NA	Toluene	Activity depends on mesostructure	[71]
3D TiO_2/Cu_2O on Cu foam	Sacrificial template, *T* not reported	3D monolith	88% activity after 4 cycles	Toluene	90.2% removal (180 min, 500 W Xe lamp)	[72]
N-doped TiO_2	Doctor-blade (sol–gel), 400 °C	1.0	NA	Toluene (2 μL)	85% removal (2 h, visible light)	[73]
TiO_2 on window glass	Ultrasonic spray pyrolysis, 350–450 °C	0.1–0.24	Adequately adhered	Methyl tert-butyl ether	80% conversion (optimal at 350 °C)	[74]
TiO_2 on fibrous filters	Spray atomization/spray gun, *T* not reported	Varying	Best with spray gun	Toluene	Activity ranked: SG > SA > SD > dip-coating	[75]
C-doped P25 coated on Ni foam	Dip-coating with ultrasonication, 150 °C	NA	NA	methyl ethyl ketone (1000 ppb)	94% degradation with 3-layers	[76]
TiO_2 Nanotubes on glass	Doctor-blade, 200 °C	10	NA	Toluene (300 ppm)	$k = 0.041\ min^{-1}$ under air	[77]
TiO_2 trapped in transparent multilayered per-fluoropolymeric coating	Casting, 50 °C	NA	NA	Pentane, methanol, 2-propanol, toluene, pyridine (2000 ppm)	$k = 0.01\ min^{-1}$	[78]
Ultrasonic assisted hydrothermal synthesis of TiO_2@MIL-101	25 mg pressed disk, *T* not reported	NA	NA	Toluene	$k = 0.0064\ min^{-1}$	[79]

NA, not available.
[a]Values estimated from figures or text.

the thermal treatment protocol of 150 °C for 1 h in a convection oven was applied across all batches (±2 °C temperature uniformity verified), and finally, 5) the number of coating passes was exactly 3 times to achieve target surface density of 1.0 mg cm^{-2}. which was verified across 3 replicate films prepared in independent batches, and the measured surface density was 1.0 ± 0.1 mg cm^{-2}, representing a relative standard deviation of 10%.

Characterization: Scratch resistance tests were done according to the ISO 15184:2012 method for determining the film hardness by using Elcometer 501 Pencil Hardness Tester (Elcometer Ltd, UK). Each sample was tested three times, that is, in three different places of the coated glass slide. Scanning electron microscopy (SEM) images were taken using Zeiss Supra 3 VP field emission gun (FEG) microscope, operating at 1 kV. Elemental composition was determined by the energy-dispersive X-ray (EDX) analysis with INCA Energy System, attached to the above-described microscope, operating at 20 kV. Transmission electron microscopy (TEM) images were obtained from a JEOL JEM 2100 HR transmission electron microscope at an accelerating voltage of 200 kV. The X-ray diffraction (XRD) patterns were obtained from a PANalytical X'pert Pro high-resolution diffractometer operated at 40 kV. CuK_α irradiation (Wavelength 1.5406 Å) was used in the range from 0.5° to 5° for small-angle range and 5° to 60° for wide-angle range with a step size of 0.033. Thermogravimetry was conducted on TGA Q5000 apparatus from TA Instruments. The samples were first heated in argon atmosphere from room temperature to 120 °C at a rate of 10 °C min^{-1}, left at this temperature for 10 min and then further heated at a rate of 20 °C min^{-1} to 800 and 500 °C for pure SiO_2 and TiO_2 samples, respectively. The calculation of the OH surface density was done by the equation:[59]

$$\#\frac{OH}{nm^2} = \alpha \frac{(\#OH/nm^2)T_2 \times SSA \times wtT_2 + \left[\frac{(wtT_1 - wtT_2)}{\frac{MW(H_2O)}{N_A}} \times 2\right]}{SSA \times wtT_1} \quad (1)$$

Where, wtT_1 is the sample weight at the corresponding temperature T_1 (120 °C), $MW(H_2O)$ is the molecular weight of water, N_A is Avogadro's constant, and α is a calibration factor in our case 0.625.(5) For silica, 1 OH nm^{-2} remains on the surface at T_2 = 800 °C, while for titania, it is assumed that at T_2 = 500 °C the powder surface is free of OH surface groups.[59] A confirmation of the higher presence of OH groups was done with XPS analysis (Figure S9, Supporting Information). X-ray photoelectron spectroscopy (XPS) measurements were conducted

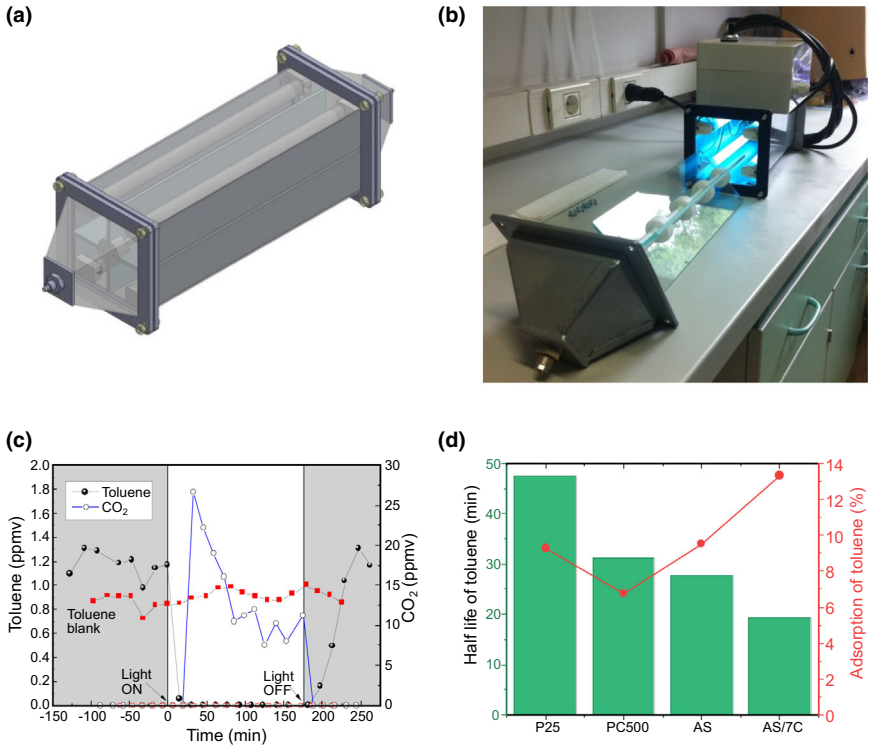

Figure 4. Showcase of application of the AS/7C composite photocatalyst with the Ti:Si molar ratio of 1:1 against degradation of toluene. A 3D model (a), and a real-life photograph (b) with temporal concentrations of toluene and CO_2 during operation (c). Flow of air through the unit was set at 400 mL min^{-1} and the inlet toluene concentration at 1 ppmv which was checked in a separate experiment noted as toluene blank (red squares in [c]). Comparison of catalytic performance of pristine titania (powder P25, powder PC500, colloidal AS) and AS/7C catalyst (d). Rection conditions: *m*(catalyst) = 1 g, rel. humidity = 50%, residence time = 0.8 min.

using a Versa Probe 3 AD (PHI, Chanhassen, USA) equipped with a monochromatic Al Kα X-ray source. The source operated at an accelerating voltage of 15 kV and an emission current of 13.3 mA. Powder samples were mounted on double-sided Scotch tape and positioned at the center of the XPS holder. Spectra were acquired for each sample over a 200 µm × 200 µm analysis area, with the charge neutralizer activated during data collection. Survey spectra were measured using a pass energy of 224 eV and a step size of 0.8 eV. High-resolution (HR) spectra were recorded with a pass energy of 27 eV and a step size of 0.05 eV. To ensure high-quality spectral data with a good signal-to-noise ratio, at least 10 sweeps were performed for each measurement. Spectral deconvolution was carried out using KherveFitting v1.65 software.

UV–vis absorption spectra (UV–vis) were measured on a LAMBDA 650 instrument equipped with an integrating sphere with 150 mm PbS detector. Fourier transform infrared spectroscopy (FT-IR) spectra were recorded on a Perkin Elmer Spectrum 100 spectrometer, using a KBr tablet method from 4000 cm^{-1} to 450 cm^{-1} with a step of 1 cm^{-1}, and attenuated total reflectance measurements (ATR-FTIR) were made on Perkin Elmer Spectrum One spectrometer in the range of 4000 to 650 cm^{-1} with a step of 1 cm^{-1}. Each spectrum was recorded 14 times. Elemental analysis was measured with inductively coupled plasma optical emission spectrometry (ICP-OES) on Varian, model 715-ES.

Nitrogen physisorption curves were measured on Tristar 3000 Micromeritics volumetric adsorption analyzer at 77 K.

Acidic properties of the materials were investigated by temperature programmed desorption of pyridine followed by IR spectroscopy (TPD-IR). Powders were pressed (2 bar) in self-supported discs (2 cm^2 area, weighing approximately 20 mg) and placed in an IR cell equipped with KBr windows, operating under primary (0.01 torr) and secondary vacuum (5×10^{-6} torr). The IR spectra were recorded using a Nicolet 5700 spectrometer from Thermo Electron Corporation (USA) in the 5500–400 cm^{-1} range at a resolution of 4 cm^{-1} and 128 scans were recorded for each spectrum. They were analyzed with OMNIC 8.2.387 software. They were normalized to 20 mg. A movable quartz sample holder allowed placing the self-supported discs in the infrared beam, for recording spectra, and moving it into a furnace at the top of the cell for thermal treatment. Pyridine (Py) adsorption was performed by introduction of doses inside the IR cell containing the previously activated (under vacuum at 473 K for 3 h) self-supported discs of the samples. After introduction of each dose of Py, the sample was heated at 473 K for 10 min to allow diffusion towards all accessible sites before recording the spectrum. Infrared spectra were recorded after Py saturation (1.33 mbar at equilibrium) followed by evacuation at 473 K to remove physiosorbed species. The deconvolution of the peaks was done using fityk 1.3.1 software.

The analyses of D_2O isotopic exchange were carried out as follows. Samples were pressed into self-supported wafer (~20 mg, 2 cm^2) and placed into a cell where activation occurred. This step consists in heating the wafer under secondary vacuum to evacuate physisorbed and chemisorbed species from the surface of the sample. They were heated at 150 °C for 3 h under secondary vacuum. After activation, an isotopic exchange is performed with D_2O, to change accessible OH groups into OD groups. Then, the sample is activated a second time at 150 °C for 3 h under secondary vacuum to remove the excess of heavy water. The samples were then exposed to bulky alcohol molecules in order to exchange accessible OD into OH to quantify the amount of OD groups accessible to a certain size of molecule. D/H exchange was first performed with largest molecules. Alcohols we used are: 3-ethylpentan-3-ol, 2-methylpropan-2-ol, propan-2-ol and methanol (Scheme S1, Supporting Information).

Catalytic Tests: Photocatalytic degradation of toluene and formaldehyde was conducted in closed-circulation lab-made system with 500 mL borosilicate cell as a photoreactor and is described in detail elsewhere.[84] Two low-pressure Hg lamps (15 W, Philips CLEO) were placed opposite to each other to assure the irradiation power of 2.47 mW cm^{-2}. The pollutants were introduced at the initial concentration of toluene and formaldehyde 50 ± 3 ppm (v/v) and 1 ± 0.1 ppm (v/v), respectively. Toluene was analyzed on-line on a Saturn 2100 T GC–MS chromatograph (Varian), whereas quantification of formaldehyde was done with HAL-HFX205 Formaldehyde meter (Hal Technology). In a typical experiment one coated glass slide was used (approximately 65 mg of catalyst), adsorption–desorption equilibrium was reached in 1 h, and irradiation phase of the experiment lasted 5 h, during which a sample to the gas chromatograph was taken every 15 min, and a sample to the formaldehyde meter was taken every 5 min. Reaction kinetics typically followed first-order ($R^2 \geq 0.96$ for toluene and $R^2 \geq 0.87$ for formaldehyde), thus apparent reaction rate constants (k_{app}) were calculated by

$$\ln(c_0/c) = k_{app} * t \quad (2)$$

where t is time, c_0 is the initial concentration of the model molecule after adsorption–desorption equilibrium has been established.

Acknowledgements

The SEM and nitrogen physisorption measurements were done by Mojca Opresnik and the XRD measurements by Edi Kranjc, both from the National Institute of Chemistry, Ljubljana, for that we are very grateful. Slovenian Research and

Innovation Agency is acknowledged for financial support via core funding programs P1-0418, P1-0134, P1-0021 and via projects J2-4444, N2-0310, GC-0003. European Cooperation in Science and Technology is also acknowledged for funding through NETPORE COST action CA20126 while European Commission is acknowledged for funding through Horizon Europe project FlowCat (grant No. 101160108).

Conflict of Interest

The authors declare no conflict of interest.

Supporting Information

Supporting Information is available from the Wiley Online Library or from the author.

Keywords

colloidal-based synthesis, material science, physicochemical stability, surface chemistry, TiO_2-SiO_2 composite films

Received: December 11, 2025
Revised: May 6, 2026
Published online: May 17, 2026

[1] C. He, J. Cheng, X. Zhang, M. Douthwaite, S. Pattisson, Z. Hao, *Chem. Rev.* **2019**, *119*, 4471.
[2] V. I. Parvulescu, F. Epron, H. Garcia, P. Granger, *Chem. Rev.* **2022**, *122*, 2981.
[3] X. Sun, S. Jiang, H. Huang, H. Li, B. Jia, T. Ma, *Angew. Chem. Int. Ed.* **2022**, *61*, 61.
[4] R. S. Pedanekar, S. V. Mohite, A. S. Jamadar, S. D. Dhas, S. B. Madake, P. K. Pawar, K. Y. Rajpure, S. J. Kim, *Appl. Mater. Today* **2026**, *48*, 103011.
[5] X.-W. Lv, X. Ding, J. Gong, X. Yan, D. Huang, J. Geng, Z.-Y. Yuan, *Acta Phys. -Chim. Sin.* **2026**, *42*, 100151.
[6] Z. Liu, R. Fan, Y. Wan, X. Zhang, S. Gao, Z. Xu, *Coord. Chem. Rev.* **2026**, *555*, 217629.
[7] C. Zhuang, C. Zhang, D. Zhang, Y. Zhang, Z. Liu, P. Shan, W. Zhang, P. Xu, S. Li, *J. Mater. Sci. Technol.* **2025**, *239*, 195.
[8] S. Tunala, S. Zhai, F. Wu, Y.-H. Chen, *Sci. China Chem.* **2025**, *68*, 3415.
[9] H. Liu, W. Xiong, C. Zhou, C. Lai, L. Li, G. Wang, X. Huo, G. Zeng, M. Cheng, *Coord. Chem. Rev.* **2025**, *529*, 216468.
[10] M. Hu, J. Alharbi, H. Zhang, H. S. Al Qahtani, C. Feng, *Chem. Res. Chin. Univ.* **2025**, *41*, 237.
[11] C. Ashina, N. Pugazhenthiran, R. V. Mangalaraja, P. Sathishkumar, *Renew. Sust. Energ. Rev.* **2025**, *214*, 115490.
[12] S. Fang, Y. H. Hu, *Chem. Soc. Rev.* **2022**, *51*, 3609.
[13] M. Coha, G. Farinelli, A. Tiraferri, M. Minella, D. Vione, *Chem. Eng. J.* **2021**, *414*, 128668.
[14] K. Yu, Z.-J. Bai, Z. Wang, G. Xie, M. Gonfa, Z. Wang, *Chem. Eng. Sci.* **2026**, *320*, 122425.
[15] J. Liu, N. Ma, W. Wu, Q. He, *Chem. Eng. J.* **2020**, *393*, 124719.
[16] A. Kumar, P. Choudhary, A. Kumar, P. H. C. Camargo, V. Krishnan, *Small* **2022**, *18*, 18.
[17] T. Wang, S. Yu, C. Wang, X. Yin, H. Niu, S. Gao, *Energy Environ. Mater.* **2026**, *9*, e70097.
[18] C. Ayappan, R. Xing, X. Zhang, D. Luo, S. Liu, A. Fujishima, *Coord. Chem. Rev.* **2024**, *515*, 215960.
[19] X. Sun, J. Tian, J. Cai, Y. Wang, T. He, X. Qiu, Z. Li, Z. Yao, D. W. Bahnemann, J. Pan, *Energy Environ. Mater.* **2025**, *8*, e70012.
[20] C. Hu, S. Tu, N. Tian, T. Ma, Y. Zhang, H. Huang, *Angew. Chem. Int. Ed.* **2021**, *60*, 16309.
[21] Z. Qiao, L. Li, B. He, Y. Zhu, Y. Chen, Y. Yang, X. Liu, *Energy Environ. Mater.* **2026**, *9*, e70245.
[22] S. He, Y. Chen, J. Fang, Y. Liu, Z. Lin, *Chem. Soc. Rev.* **2025**, *54*, 2154.
[23] Y. Nosaka, A. Y. Nosaka, *Chem. Rev.* **2017**, *117*, 11302.
[24] J. N. Schrauben, R. Hayoun, C. N. Valdez, M. Braten, L. Fridley, J. M. Mayer, *Science* **2012**, *336*, 1298.
[25] Z. Zhao, C. S. Law, A. Santos, *Energy Environ. Mater.* **2026**, DOI: 10.1002/eem2.70353
[26] Z. Shayegan, C.-S. Lee, F. Haghighat, *Chem. Eng. J.* **2018**, *334*, 2408.
[27] H. Dong, G. Zeng, L. Tang, C. Fan, C. Zhang, X. He, Y. He, *Water Res.* **2015**, *79*, 128.
[28] A. Šuligoj, R. Cerc Korošec, G. Žerjav, N. Novak Tušar, U. Lavrenčič Štangar, *Top. Curr. Chem.* **2022**, *380*, 51.
[29] X. Yu, T. J. Marks, A. Facchetti, *Nat. Mater.* **2016**, *15*, 383.
[30] Q. Lu, Z. Yang, X. Meng, Y. Yue, M. A. Ahmad, W. Zhang, S. Zhang, Y. Zhang, Z. Liu, W. Chen, *Adv. Funct. Mater.* **2021**, *31*, 31.
[31] U. L. Štangar, U. Černigoj, P. Trebše, K. Maver, S. Gross, *Mon. Chem.—Chem. Mon.* **2006**, *137*, 647.
[32] R. Fateh, R. Dillert, D. Bahnemann, *ACS Appl. Mater. Interfaces* **2014**, *6*, 2270.
[33] W. Hu, L. Yang, P. Shao, H. Shi, Z. Chang, D. Fang, Y. Wei, Y. Feng, Y. Huang, K. Yu, X. Luo, *Environ. Sci. Technol.* **2022**, *56*, 10412.
[34] K. Hua, Z. Wu, W. Chen, X. Xi, X. Chen, S. Yang, P. Gao, Y. Zheng, *Molecules* **2024**, *29*, 4391.
[35] Y. Ren, W. Li, Z. Cao, Y. Jiao, J. Xu, P. Liu, S. Li, X. Li, *Appl. Surf. Sci.* **2020**, *509*, 145377.
[36] T. Zimmermann, C. Fischer, M. Oppmann, S. Wenderoth, B. Winzer, F. Somorowsky, N. Vogel, K. Mandel, S. Wintzheimer, *ACS Appl. Nano Mater.* **2025**, *8*, 4087.
[37] I. Nabi, A.-U.-R. Bacha, K. Li, H. Cheng, T. Wang, Y. Liu, S. Ajmal, Y. Yang, Y. Feng, L. Zhang, *iScience* **2020**, *23*, 101326.
[38] C. Liu, J. Qian, Y. Ye, H. Zhou, C.-J. Sun, C. Sheehan, Z. Zhang, G. Wan, Y.-S. Liu, J. Guo, S. Li, H. Shin, S. Hwang, T. B. Gunnoe, W. A. Goddard, S. Zhang, *Nat. Catal.* **2020**, *4*, 36.
[39] S. Yaparatne, C. P. Tripp, A. Amirbahman, *J. Hazard. Mater.* **2018**, *346*, 208.
[40] S. Latthe, S. Liu, C. Terashima, K. Nakata, A. Fujishima, *Coatings* **2014**, *4*, 497.
[41] A. Šuligoj, U. L. Štangar, A. Ristić, M. Mazaj, D. Verhovšek, N. N. Tušar, *Appl. Catal. B Environ.* **2016**, *184*, 119.
[42] T. N. Obee, R. T. Brown, *Environ. Sci. Technol.* **1995**, *29*, 1223.
[43] M. Tasbihi, U. Lavrenčič Štangar, A. S. Škapin, A. Ristić, V. Kaučič, N. Novak Tušar, *J. Photochem. Photobiol. A Chem.* **2010**, *216*, 167.
[44] J. C. Brinker, G. W. Scherer, *Sol-Gel Science: The Physics and Chemistry of Sol-Gel Processing*, 1st ed., Academic Press, San Diego, USA **1990**.
[45] M. Shen, M. Wang, Q. Wang, J. Tian, L. Zhang, L. Wang, J. Shi, *Chem. Eng. J.* **2021**, *425*, 131513.
[46] C. Ribeiro, C. M. Costa, D. M. Correia, J. Nunes-Pereira, J. Oliveira, P. Martins, R. Gonçalves, V. F. Cardoso, S. Lanceros-Méndez, *Nat. Protoc.* **2018**, *13*, 681.
[47] J. Du, W. Wang, M. Wan, X. Wang, G. Li, Y. Tan, C. Li, S. Tu, Y. Sun, *Adv. Energy Mater.* **2021**, *11*, 2102259.
[48] Occupational Safety and Health Administration (OSHA), Occupational Safety and Health Standards, Toxic and Hazardous Substances. **1998**.
[49] U.S. Environmental Protection Agency, Integrated Risk Information System (IRIS) on Toluene, National Center for Environmental Assessment, Office of Research and Development, Washington, D.C. **2005**.
[50] A. Šuligoj, I. Arčon, M. Mazaj, G. Dražić, D. Arčon, P. Cool, U. L. Štangar, N. N. Tušar, *J. Mater. Chem. A* **2018**, *6*, 9882.
[51] S. Kermadi, N. Agoudjil, S. Sali, L. Zougar, M. Boumaour, L. Broch, A. En Naciri, F. Placido, *Spectrochim. Acta A Mol. Biomol. Spectrosc.* **2015**, *145*, 145.
[52] O. d'Hennezel, P. Pichat, D. F. Ollis, *J. Photochem. Photobiol. A Chem.* **1998**, *118*, 197.

[53] A. Fujishima, X. Zhang, D. A. Tryk, *Surf. Sci. Rep.* **2008**, *63*, 515.
[54] A. Carretero-Genevrier, C. Boissiere, L. Nicole, D. Grosso, *J. Am. Chem. Soc.* **2012**, *134*, 10761.
[55] D. R. Ramos, M. Iazykov, M. I. Fernandez, J. A. Santaballa, M. Canle, *Front. Chem. Eng* **2021**, *3*, 688498.
[56] G. Ricchiardi, A. Damin, S. Bordiga, C. Lamberti, G. Spanò, F. Rivetti, A. Zecchina, *J. Am. Chem. Soc.* **2001**, *123*, 11409.
[57] S. Klein, *J. Catal.* **1996**, *163*, 476.
[58] M. Yoshikawa, H. Seki, K. Inoue, T. Kobayashi, T. Kimoto, *Appl. Spectrosc.* **2017**, *71*, 911.
[59] R. Mueller, H. K. Kammler, K. Wegner, S. E. Pratsinis, *Langmuir* **2003**, *19*, 160.
[60] L. Wang, R. T. Yang, *J. Phys. Chem. C* **2011**, *115*, 21264.
[61] M. Ide, M. El-Roz, E. De Canck, A. Vicente, T. Planckaert, T. Bogaerts, I. Van Driessche, F. Lynen, V. Van Speybroeck, F. Thybault-Starzyk, P. Van Der Voort, *Phys. Chem. Chem. Phys.* **2013**, *15*, 642.
[62] D. Kumar, K. Schumacher, C. du Fresne von Hohenesche, M. Grün, K. K. Unger, *Colloids Surf. A Physicochem. Eng. Asp.* **2001**, *187–188*, 109.
[63] A. C. Y. Liu, A. E. D. Bøjesen, A. R. F. Tabor, A. S. T. Mudie, A. A. Zaccone, A. P. Harrowell, A. T. C. Petersen, *Sci. Adv.* **2022**, *8*, eabn0681.
[64] D. Grégori, I. Benchenaa, F. Chaput, S. Thérias, J.-L. Gardette, D. Léonard, C. Guillard, S. Parola, *J. Mater. Chem. A* **2014**, *2*, 20096.
[65] J. Balajka, M. A. Hines, W. J. I. DeBenedetti, M. Komora, J. Pavelec, M. Schmid, U. Diebold, *Science* **2018**, *361*, 786.
[66] J. P. Gallas, J. M. Goupil, A. Vimont, J. C. Lavalley, B. Gil, J. P. Gilson, O. Miserque, *Langmuir* **2009**, *25*, 5825.
[67] T. Daubert, R. Danner, *Physical and Thermodynamic Properties of Pure Chemicals: Data Compilation, Part 1*, Taylor & Francis, Washington, USA **1989**.
[68] S. Rahmadani, A. Anawati, *Appl. Surf. Sci. Adv.* **2024**, *23*, 100631.
[69] K. Boubaker, *The European Physical Journal Plus* **2011**, *126*, 10.
[70] N. Negishi, S. Matsuzawa, K. Takeuchi, P. Pichat, *Chem. Mater.* **2007**, *19*, 3808.
[71] F. Bosc, D. Edwards, N. Keller, V. Keller, A. Ayral, *Thin Solid Films* **2006**, *495*, 272.
[72] S. Chen, L. Zhang, S. Melhi, D. A. Alshammari, M. A. Amin, L. Dai, S. Li, W. Yu, L. Cui, *Adv. Compos. Hybrid Mater.* **2024**, *7*, 250.
[73] Y. Y. Kannangara, R. Wijesena, R. M. G. Rajapakse, K. M. N. De Silva, *Int. Nano Lett.* **2018**, *8*, 31.
[74] I. Dundar, M. Krichevskaya, A. Katerski, M. Krunks, I. Oja Acik, *Catalysts* **2019**, *9*, 915.
[75] S. Drdova, M. Giannakou, F. Jiang, L. Lin, D. Sivaraman, R. Toth, T. Graule, A. Braun, J. Ilavsky, I. Kuzmenko, J. Wang, *Front. Chem.* **2022**, *10*, 887431.
[76] Z. Shayegan, F. Haghighat, C.-S. Lee, *J. Environ. Chem. Eng.* **2020**, *8*, 104162.
[77] S. Weon, J. Kim, W. Choi, *Appl. Catal. B Environ.* **2018**, *220*(5), 1.
[78] M. Sansotera, S. Geran Malek Kheyli, A. Baggioli, C. L. Bianchi, M. P. Pedeferri, M. V. Diamanti, W. Navarrini, *Chem. Eng. J.* **2019**, *361*, 885.
[79] X. Zhang, Z. Zhu, R. Rao, J. Chen, X. Han, S. Jiang, Y. Yang, Y. Wang, L. Wang, *J. Environ. Sci.* **2023**, *134*, 21.
[80] N. N. Tušar, A. Ristić, G. Mali, M. Mazaj, I. Arčon, D. Arčon, V. Kaučič, N. Z. Logar, *Chem. Eur. J.* **2010**, *16*, 5783.
[81] M. Mazaj, W. J. J. Stevens, N. Z. Logar, A. Ristić, N. N. Tušar, I. Arčon, N. Daneu, V. Meynen, P. Cool, E. F. Vansant, V. Kaučič, *Microporous Mesoporous Mater.* **2009**, *117*, 458.
[82] H. E. Bergna, W. O. Roberts, *Colloidal Silica: Fundamentals and Applications*, CRC Press, Boca Raton, USA **2006**.
[83] J. Wang, M. Liang, Y. Fang, T. Qiu, J. Zhang, L. Zhi, *Adv. Mater.* **2012**, *24*, 2874.
[84] M. Tasbihi, M. Kete, A. M. Raichur, N. N. Tušar, U. L. Štangar, *Environ. Sci. Pollut. Res.* **2012**, *19*, 3735.